Available online at www.sciencedirect.com

SCIENCE @ DIRECT®

ELSEVIER

Journal of Nuclear Materials 325 (2004) 61–77

journal of nuclear materials

www.elsevier.com/locate/jnucmat

The development of grain-face porosity in irradiated oxide fuel

R.J. White *

RW Consulting, 18 Green Close, Uley, Dursley, Gloucestershire GL11 5TH, UK

Received 9 September 2003; accepted 31 October 2003

Abstract

The predominant mode of fission gas release occurs through atomic diffusion to the grain boundaries. In oxide fuels the fission gases initially precipitate as an array of small lenticular bubbles of circular projection. The arrival of additional gas and vacancies causes these bubbles to grow and coalesce into fewer, larger bubbles. Depending on the irradiation conditions and temperatures, these bubbles may develop either as circular lenticular pores or as extended multi-lobed pores. Eventually the pores may intersect the grain edges where pathways may be formed which enable the gas to migrate to the outer geometry of the fuel and hence to the gap and the pin free volume. Recent extensive PIE campaigns on irradiated fuels have provided a large database of inter-granular porosity development and, from these, models of bubble growth, coalescence, morphological relaxation and venting have been developed.

1. Introduction

The generation of the fission gases, xenon and krypton, in irradiated fuel presents a number of problems to reactor operators. If the gases remain within the fuel matrix they may produce large transient swelling under adverse operational conditions. Alternatively, release to the pin free volume can lead to deterioration of the fuel thermal performance, escalating release and possible rod over-pressure events. In order that proper safety assessments may be made it is essential that the processes that determine the release or retention of fission gases are properly understood.

Probably the key determinant in this is the kinetics of grain-face bubble development. Observations of lightly irradiated fuel reveal large numbers of small, discrete, lenticular bubbles on the planar boundaries (faces). With further irradiation, the size of the bubbles increase and their numbers decrease. At some stage the bubbles may depart from pure circular projection, become elongated and frequently multi-lobal. During this period the bubbles remain closed cavities and act to retain the fission gases on the boundaries, thereby contributing to large swellings. The development of elongated pores eventually results in the bubbles making contact with the grain edges – where three grains meet – and this can lead to the development of continuous pathways to the fuel exterior through which the gases may be vented. The final stage in the process is the inter-connection of all the porosity on the grain faces to the grain edges and from this point, all gas arriving at the boundaries will be released.

In this paper, the concepts of growth, coalescence, morphological relaxation and venting of grain-face porosity are examined in relation to recent PIE studies of irradiated fuel.

2. The fuel swelling database

Experiments conducted by British Energy have been directed at providing a better understanding of the processes contributing to fuel swelling in irradiated oxide fuels. The British Energy programme involved the ramping of Advanced Gas Cooled Reactor UO_2 fuel (CAGR) in the Halden Reactor using fuels that were base-irradiated in the Hinkley Point, Torness and Halden Reactors up to burn-ups of around 21 GWd/t U.

The fuel from all the experiments was returned to Magnox Electric's Shielded Electron Optics Suite at

---

* Tel.: +44-1453 860046.

E-mail address: fuelrod@btinternet.com (R.J. White).

0022-3115/$ - see front matter © 2003 Elsevier B.V. All rights reserved.
doi:10.1016/j.jnucmat.2003.10.008

Table 1
Details of PIE/SEM performed

Test	Burn-up (GWd/t U)	Ramp type	Peak rating (kW/m)	Hold-time	Temperature zones	Boundaries measured	Bubbles measured
4000	20.7	Fast	40	30 min	5	48	5043
4004	20.5	Fast	40	2 min	6	44	8010
4005	20.8	Fast	40	2 min	5	39	5031
4064	20.1	Slow	43	–	5	63	6704
4065	9.3	Slow	41.8	–	5	43	2817
4159	20.2	Cycled	18–26	115×4 h	5	56	3391
4160	20.1	Cycled	18–26	115×4 h	7	50	2794
4162	12.6	Slow	40	–	4	47	12 031
4163	12.6	Fast	40	2 min	5	37	10 596
					47	427	56 417

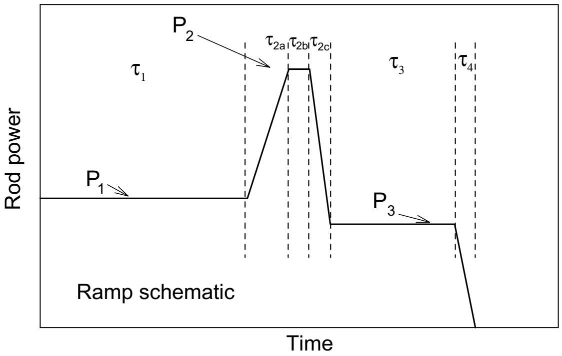

Fig. 1. Schematic of terminal ramps in the CAGR/Halden tests. The parameters for each individual ramp are tabulated in Table 2.

Berkeley (UK) where extensive scanning electron microscopy was performed to study both intra-granular and inter-granular swellings. A complete study of both intra- and inter-granular porosity was performed and the results of these have recently been reported [1] and made available for general use through the OECD Fuel Performance Database [2]. Brief details of the different tests performed are given in Table 1.

The specimens reported here were subjected to either ramps – designated fast or slow – or power cycling. The schematic form of the ramp is shown in Fig. 1 and the times and powers of each stage are summarised in Table 2. Note that the slow ramps are those in which τ_{2a} is of the order of 45 min and the fast ramps are those for which τ_{2a} is from 1–2 min.

The two power-cycled specimens were subjected to 115 four-hour cycles, the details of which are summarised in Table 3.

The fuel rods were encased in a Zircaloy shroud for irradiation in the Halden Reactor and the interspace was pre-filled (usually) with helium although a mixture of helium and argon was employed in one of the power-cycled rods, which resulted in higher cladding temperatures and consequently higher fuel temperatures.

Although the information reported here originates from fuel of relatively modest burnups, the physical processes of swelling and gas release are unlikely to change greatly until burnups of 45–50 GWd/t U are exceeded when changes in the fuel microstructure, for example, grain refinement begin to occur. Even then only a small fraction of fuel near the periphery is likely to be affected and the predominant release and swelling processes will be similar to those operating at lower burnups. An additional criticism can be levelled at the

Table 2
Details of power ramps – fast and slow ramps

SEM/ TEM identifier	Ramp rig	Power 1 kW/m	τ_1	τ_{2a} (min)	Power 2 kW/m	τ_{2b} (min)	τ_{2c} (s)	Power 3 kW/m	τ_3 (min)	τ_4
4000	583.2/2	14.0	12d	1.52	40.0	30.0	100	14.0	99.0	SCRAM
4004	583.2/4	14.0	12d	1.97	40.0	2.38	90	14.0	99.0	
4005	583.2/1	14.0	12d	1.32	40.0	2.0		SCRAM		
4064	583.4/3	20.0	15wk	47.0	43.0	0.0		SCRAM		
4065	576.4/6	19.3	3wk	47.0	41.8	0.0		SCRAM		
4162	587.4/1	18.0	3wk	45.0	40.0	0.0	40	18.0	6	
4163	587.4/3	18.0	3wk	1.0	40.0	2.0		SCRAM		

Table 3
Details of power ramps – power-cycling cases

SEM/TEM identifier	Ramp rig	Power 1 kW/m	Time 1	Ramp up	Power up kW/m	Ramp Dn	Power Dn kW/m	DeCond kW/m	Time	And after?
4159 and 4160	619.2/2 and /4	18	7d	115–4 h cycles				18	2d	Shut-down
				30 min	26 for 1 h	30 min	18 for 2 h			

fact that the irradiations were performed under AGR rather than LWR conditions. The main difference is associated with the magnitudes of the hydrostatic stresses operating in the fuel types but it is shown later that these are second-order effects in the swelling process.

2.1. PIE measurements

The area, perimeter and number of lobes to each bubble were measured using image analysis software. The basic assumption that the volume of a bubble may be related to an idealised bubble with equivalent perimeter and area. The relationships between the bubble dimensions and swelling are given in the Appendix A for lenticular bubbles of the dimensions observed in irradiated UO_2 and post-processing of the data provided the following information for each boundary:

(i) Grain-face area, A_{gb}.
(ii) Number of discrete pores, N_b.
(iii) Bubble density (number per unit area), $N = N_b/A_{gb}$.
(iv) Fractional coverage of grain face by porosity (by area), F_c.
(v) Volumetric swelling, $\Delta V/V$ (%).
(vi) Mean projected bubble radius (not radius of curvature) and frequency distributions, R_p.
(vii) Mean projected bubble body length and frequency distributions, L_p.
(viii) Mean number of lobes ($=2$ for circles and bilobes) and frequency distributions, N_L.
(ix) Vented fraction (fraction or area covered which is vented to grain edges), F_v.

The temperatures of the separate SEM locations were obtained from ENIGMA [3] calculations and ranged from 1200 to 1920 °C. These data are given in detail in [1] and a summary of the measurements is given in Table 4.

3. General behaviour

Examples of typical grain-face swelling behaviour are shown in Figs. 2–4. Fig. 2 shows an example of the very early stages of bubble development and the bubble density is high with little evidence of departures from circular bubbles. In contrast, Fig. 3 shows the results of extensive bubble coalescence and a much reduced bubble density. Finally, Fig. 4 shows the presence of extended pores with a high degree of bubble venting, that is, the bubbles terminate on the grain edges.

From a detailed study of the database, the following observations may be made:

(i) The number density of grain-face pores falls as the bubble size increases.
(ii) The fraction of the area of the grain boundaries covered by bubbles increases to a limiting value of around 50% although values as high as 60% are not uncommon.
(iii) The degree of lobality, that is, the mean length to radius ratio (L_p/R_p) of the bubbles increases with fractional coverage, sometimes exceeding values of 20.
(iv) The fraction of vented pores is a function of mean bubble length L_p.

4. The physical basis of grain-boundary swelling

The mechanistic development of grain-face swelling may be conveniently subdivided into the following effects:

(a) The nucleation of grain-face cavities/pores/bubbles.
(b) The growth of twofold symmetric cavities on planar grain boundaries (faces) through the collection of fission gas atoms and vacancies.
(c) The rate at which cavities interact through coalescence leading to larger but fewer bubbles.
(d) The change of shape of newly coalesced cavities under the influence of capillarity.
(e) The kinetics of venting of the grain-face porosity to the grain edges.

These are discussed below.

4.1. Cavity nucleation

The measured bubble densities ranged from in excess of 40 to fewer than 0.04 bubbles per μm^2 of grain

Table 4
Summary of derived swelling data from ramp tests

Section	Temperature (°C)	Nb/Agb (μm^{-2})	$\Delta V/V$ (%)	R_p (μm)	L_p (μm)	F_c (%)	F_v (%)	$\langle N_L \rangle$
4000-A	1775	0.68 ± 0.46	0.99 ± 0.36	0.22 ± 0.04	1.18 ± 0.53	43.0 ± 6.0	54.1 ± 12.0	4.2
4000-B	1743	0.80 ± 0.17	0.76 ± 0.13	0.22 ± 0.03	0.47 ± 0.24	30.2 ± 3.8	20.4 ± 11.5	2.6
4000-C	1701	1.32 ± 0.24	0.54 ± 0.10	0.18 ± 0.02	0.29 ± 0.10	27.8 ± 4.0	8.2 ± 3.8	2.3
4000-D	1620	1.99 ± 0.55	0.44 ± 0.10	0.15 ± 0.01	0.36 ± 0.23	30.8 ± 5.2	9.9 ± 5.4	2.3
4000-F	1460	9.00 ± 1.13	0.18 ± 0.04	0.08 ± 0.02	0.04 ± 0.04	24.1 ± 0.8		2.0
4004-A	1807	1.39 ± 0.32	0.77 ± 0.16	0.20 ± 0.03	0.31 ± 0.21	33.4 ± 6.2	22.6 ± 11.6	2.3
4004-B	1795	2.12 ± 0.90	0.75 ± 0.28	0.15 ± 0.04	0.44 ± 0.23	39.3 ± 6.9	18.8 ± 18.1	3.0
4004-C	1756	3.55 ± 1.18	0.44 ± 0.12	0.13 ± 0.02	0.18 ± 0.22	30.0 ± 5.8	4.3 ± 2.4	2.1
4004-D	1693	1.88 ± 0.84	0.60 ± 0.16	0.14 ± 0.01	0.90 ± 0.96	39.9 ± 7.5	40.5 ± 40.1	3.2
4004-E	1605	8.50 ± 1.55	0.29 ± 0.07	0.07 ± 0.01	0.22 ± 0.03	36.7 ± 5.1		2.0
4004-F	1558	27.90	0.16	0.04	0.11	36.8		2.0
4005-A	1807	1.21 ± 0.50	1.06 ± 0.18	0.21 ± 0.02	0.50 ± 0.23	39.2 ± 5.9	25.4 ± 14.0	2.9
4005-B	1789	2.93 ± 0.97	0.65 ± 0.22	0.13 ± 0.02	0.28 ± 0.23	34.7 ± 8.3	26.0 ± 17.3	3.1
4005-C	1745	2.57 ± 0.98	0.51 ± 0.15	0.12 ± 0.02	0.49 ± 0.46	32.9 ± 8.5	17.9 ± 11.0	3.2
4005-D	1660	2.62 ± 1.25	0.62 ± 0.17	0.11 ± 0.02	0.71 ± 0.24	43.8 ± 6.3	40.6 ± 21.5	3.8
4005-E	1538	10.62 ± 2.15	0.31 ± 0.02	0.06	0.25 ± 0.04	41.7 ± 2.2		2.2
4064-A	1869	0.95 ± 0.49	1.09 ± 0.59	0.27 ± 0.07	0.76 ± 0.71	40.7 ± 11.5	47.2 ± 38.4	2.9
4064-B	1853	0.87 ± 0.44	0.89 ± 0.33	0.25 ± 0.05	0.66 ± 0.54	37.0 ± 6.7	23.0 ± 15.0	2.6
4064-C	1807	1.35 ± 0.73	0.64 ± 0.36	0.22 ± 0.07	0.82 ± 1.25	32.1 ± 8.0	19.2 ± 12.	2.8
4064-D	1732	0.74 ± 0.31	0.70 ± 0.18	0.20 ± 0.02	1.66 ± 0.81	45.3 ± 7.7		6.3
4064-E	1624	3.50 ± 1.35	0.48 ± 0.21	0.13 ± 0.05	0.50 ± 0.24	45.9 ± 5.3		3.2
4065-A	1922	0.25 ± 0.08	1.24 ± 0.43	0.28 ± 0.02	2.38 ± 0.66	49.7 ± 7.4	81.9 ± 10.1	6.3
4065-B	1906	0.37 ± 0.08	1.14 ± 0.25	0.30 ± 0.04	1.50 ± 0.36	49.5 ± 5.5	46.4 ± 18.6	3.5
4065-C	1868	0.49 ± 0.24	1.02 ± 0.28	0.24 ± 0.04	1.60 ± 0.74	44.3 ± 7.0	58.3 ± 18.7	4.3
4065-D	1805	0.88 ± 0.35	0.75 ± 0.14	0.16 ± 0.03	1.38 ± 0.76	44.8 ± 6.0		4.2
4065-E	1678	4.07	0.21	0.12		16.0		2.0
4159-A	1310–1362	0.20 ± 0.06	1.62 ± 0.20	0.43 ± 0.04	2.57 ± 1.74	51.8 ± 5.7	44.1 ± 28.1	3.2
4159-B	1306–1357	0.33 ± 0.10	1.52 ± 0.23	0.36 ± 0.05	1.30 ± 0.69	50.3 ± 5.1	35.7 ± 24.4	2.6
4159-C	1286–1336	0.28 ± 0.18	1.43 ± 0.17	0.33 ± 0.03	2.95 ± 1.87	50.0 ± 3.6	44.0 ± 24.5	4.2
4159-D	1250–1298	0.38 ± 0.08	1.03 ± 0.14	0.27 ± 0.03	1.94 ± 0.74	45.8 ± 3.7	36.8 ± 19.4	3.5
4159-E	1200–1246	0.64 ± 0.24	0.83 ± 0.26	0.31 ± 0.05	0.73 ± 1.04	33.0 ± 7.5	21.2 ± 26.0	2.6
4160-A	1438–1515	0.10 ± 0.05	2.75 ± 0.60	0.59 ± 0.06	3.15 ± 1.35	47.5 ± 6.5	70.8 ± 12.1	2.8
4160-B	1433–1510	0.09 ± 0.05	2.39 ± 0.58	0.56 ± 0.06	3.36 ± 1.24	43.8 ± 7.5	51.7 ± 36.1	2.9
4160-C	1411–1487	0.10 ± 0.04	2.31 ± 0.32	0.59 ± 0.03	3.76 ± 1.63	47.5 ± 1.8	71.8	2.9
4160-D	1370–1446	0.19 ± 0.06	1.61 ± 0.19	0.47 ± 0.06	1.96 ± 1.94	39.3 ± 4.9	55.6 ± 38.0	2.1
4160-E	1311–1385	0.23 ± 0.09	1.42 ± 0.24	0.42 ± 0.04	1.77 ± 1.14	39.4 ± 5.3	29.2 ± 20.6	2.9
4160-F	1235–1307	0.79 ± 0.43	0.89 ± 0.11	0.24 ± 0.02	0.95 ± 1.05	37.2 ± 5.2		2.5
4160-G	1184–1254	1.37 ± 0.34	0.47 ± 0.15	0.19 ± 0.03	0.16 ± 0.17	24.1 ± 6.2		2.3
4162-A	1798	3.15 ± 0.78	0.91 ± 0.33	0.15 ± 0.02	0.15 ± 0.13	37.1 ± 8.9		2.1
4162-B	1789	3.97 ± 1.27	0.60 ± 0.22	0.12 ± 0.02	0.13 ± 0.33	28.1 ± 7.7	6.32 ± 6.2	2.3
4162-C	1760	4.92 ± 1.50	0.61 ± 0.25	0.13 ± 0.03	0.12 ± 0.38	30.4 ± 7.9	1.48 ± 2.36	2.0
4162-D	1698	5.39 ± 1.39	0.48 ± 0.24	0.11 ± 0.01	0.06 ± 0.08	27.7 ± 5.6	6.43 ± 11.14	2.0
4163-A	1804	2.63 ± 0.73	0.71 ± 0.24	0.15 ± 0.02	0.22 ± 0.21	34.4 ± 8.7	12.6 ± 12.7	2.7
4163-B	1796	3.56 ± 0.82	0.61 ± 0.18	0.14 ± 0.01	0.09 ± 0.15	32.0 ± 5.1	3.2 ± 1.0	2.2
4163-C	1764	5.19 ± 1.50	0.41 ± 0.12	0.12 ± 0.02	0.09 ± 0.15	30.2 ± 6.4	0.0	2.1
4163-D	1709	5.71 ± 2.06	0.39 ± 0.06	0.10 ± 0.01	0.27 ± 0.32	36.1 ± 6.4	2.8 ± 5.6	2.2
4163-F	1624	20.40 ± 15.4	0.24 ± 0.12	0.07 ± 0.02	0.03 ± 0.02	26.1 ± 5.8		2.0

boundary. The observed reduction in bubble numbers with increased bubble size noted above, suggests that the upper figure is associated with the earlier stages of gas release and swelling. Very small intra-granular pores of around 1 nm in diameter are observed in irradiated UO_2 with concentrations of typically 10^{23}–10^{24} m^{-3} [4]. Assuming these are uniformly distributed, a fraction will be nucleated within one bubble radius of the grain

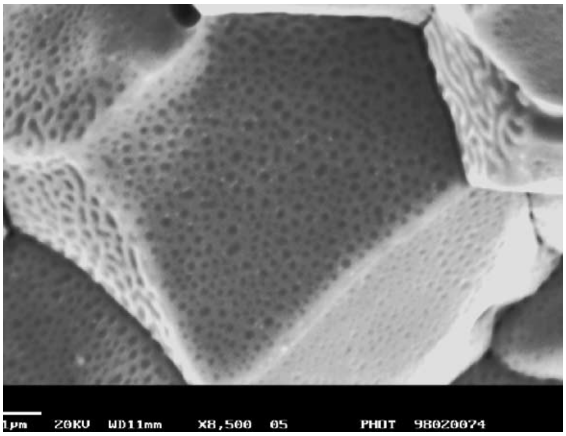

Fig. 2. An example of the relatively early stages of grain-boundary swelling with approximately circular pores. The burnup was ≃13 GWd/t U and the fuel was fast ramped and held at a temperature of about 1700 °C for 2 min. The mean projected bubble radius is 85 nm, there are approximately 9 bubbles per μm^2 of boundary and the fractional coverage is 24%. The volumetric swelling is about 0.2%. Note that some coalescence and bubble lengthening has occurred even under these conditions.

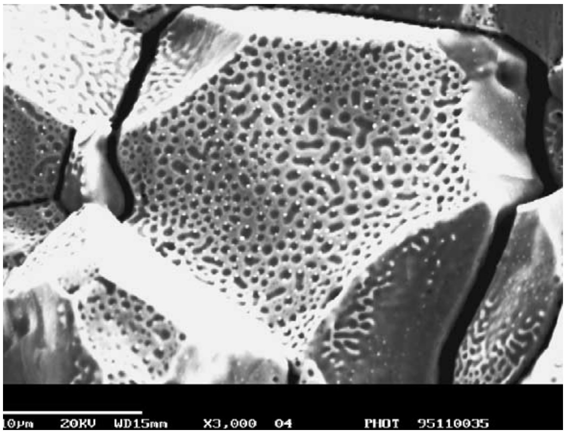

Fig. 3. An example of moderate grain-boundary porosity development. The burnup was 21 GWd/t U and the fuel was fast-ramped and held at a temperature of 1800 °C for 2 min. The mean projected radius is 220 nm, there are 1.3 bubbles per μm^2, the fractional coverage is 29% and the volumetric swelling is 0.7%. The average bubble length was 180 nm.

boundary. Any slight growth will result in their intersecting the boundary and thereof the bubbles grow as grain-face cavities. The intra-granular concentrations are therefore consistent with something between 50 and 500 bubbles per μm^2 of grain boundary. The proximity of the lower estimate with the upper value of the observed bubble numbers suggests that this may be the origin of the grain-face cavities.

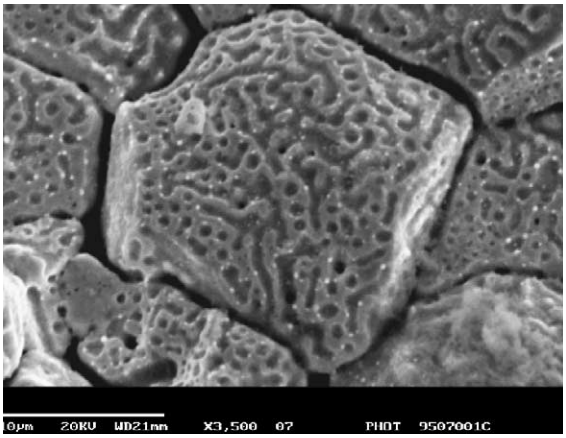

Fig. 4. Advanced development of grain-boundary porosity: this fuel was ramped under similar conditions to that in Fig. 4 but maintained at 1800 °C for 30 min. In this case the mean projected radius is 260 nm, the mean projected length is 1340 nm, there are 0.43 bubbles per μm^2, the fractional coverage is 44% and the volumetric swelling is 1.03%. Examples of multi-lobed pores and vented pores are clearly evident. Approximately 40% of the porosity is vented, that is 60% of the porosity (by area) is closed.

Because the intra-granular pores are nucleated almost continuously, it might be expected that the nucleation of grain-boundary cavities would also continue. However, once growth and coalescence of these cavities occurs, the geometric size of the initial population would tend to absorb any newly nucleated bubbles giving the effect that the nucleation was a one-off process.

4.2. Cavity growth

Fission gas atoms diffuse to the grain boundaries and are rapidly absorbed into the bubble nuclei that have formed. It is assumed that the gas retention capacity of the grain boundaries is mainly a result of the presence of the bubbles. Mechanical equilibrium requires that the pressure of the gas in the cavity is balanced by the bubble capillarity, that is $p = 2\gamma_{fs}/R$ where γ_{fs} is the UO_2/gas specific surface energy and R is the principal radius of curvature of the spherical caps which constitute the bubble/solid interfaces. This surface energy differs from that of a UO_2/UO_2 interface and this results in lenticular bubbles with a semi-dihedral angle of approximately 50° [5].

Van Uffelen [6] has considered the migration of fission gas atoms on grain boundaries from a steady state solution of the relevant diffusion equation. Since this approach assumes that the fission gas atom concentrations on the boundaries remain invariant, the solution is equivalent to instantaneous absorption of gas atoms at the cavities since the absorption rate at the cavities must equal the diffusion rate to the boundaries. A more accurate solution could be obtained by a solution of the full time-dependent diffusion equation but numerical solutions indicate this to be an unnecessary refinement.

In general, the grain-face cavities are over-pressurised and mechanical equilibrium can only be restored if the cavities can absorb vacancies. The Speight and Beere [7] model is a refinement of that originally proposed by Hull and Rimmer [8] who demonstrated how cavity growth (and shrinkage) proceeds by absorption of vacancies generated on the grain boundaries. The vacancy absorption/emission rate at a lenticular cavity of circular projection is given by

$$\frac{dn_v}{dt} = \frac{2\pi D_g \delta_g}{kTS}\left(\sigma + p - \frac{2\gamma_{fs}\sin\theta}{R_p}\right), \tag{1}$$

where

$$S = -((3 - F_c)\cdot(1 - F_c) + 2\ln(F_c))/4,$$

where n_v is the number of vacancies, D_g is the grain-boundary diffusivity, δ_g is the thickness of the diffusion layer on the boundary and σ is an externally applied stress. F_c is the fractional coverage of the circular diffusion cell by the lenticular pore. The radius, R_p, given in Eq. (1) is the projected radius of the cavity on the grain boundary and is related to the radius of curvature of the cavity through the sine of the semi-dihedral angle, θ. p is the internal pressure in the cavity and for a Van der Waal's gas is given by

$$p = \frac{kT}{\Omega\varepsilon}, \tag{2}$$

where ε is the number of vacancies per fission gas atom in the cavity, Ω is the atomic (vacancy) volume and kT is the thermal energy.

When considering cavity growth in irradiated UO_2 it is important to note that the number of cavities is decreasing so any particular bubble observed during PIE will be the result of the growth and coalescence of many other smaller bubbles. Taking the extreme example cited above, with a bubble density of 0.04 per μm^2, the originally nucleated state consisted of perhaps 40 bubbles per μm^2 so every bubble consists of 1000 of the originally nucleated seed bubbles.

Eqs. (1) and (2) concern the growth of a bubble of circular projection in a circular diffusion cell where the fractional coverage is F_c. However, finite difference calculations using elongated bubbles indicate that the equation can also be used for the case of non-circular bubbles as long as the 'S' parameter is defined in terms of the fractional coverage rather than in terms of the radii of the cavity and diffusion cells.

The overall cavity growth rate may be calculated from the numbers of vacancies and gas atoms present. For example, a cavity of volume, V, comprises n_g fission gas atoms and n_v vacancies, hence,

$$V = n_g b + n_v\Omega, \tag{3}$$

where b is the Van der Waal's volume of a fission gas atom. The overall growth rate is therefore determined by the individual rates of change of the fission gas and vacancy numbers in the cavity. The growth of grain-boundary cavities is fully interactive because the addition of fission gas atoms gives rise to a change in the pressure in the cavity via Eq. (2), or through whatever equation of state is deemed most suitable. This change in pressure immediately affects the propensity of the cavity to absorb (or emit) vacancies through the use of Eq. (1).

4.3. Bubble coalescence

Coalescence is a geometric phenomenon. Whatever the starting value of the bubble density, bubble growth will eventually lead to mechanical interference and coalescence. Given that each bubble consists of vacancies and gas atoms, the coalescence event must conserve the volume of the interacting bubbles unless the event takes place near the grain edge where venting may occur. Since each grain face has a finite area, each bubble is limited to a fraction of that area before interference occurs. The key parameter in coalescence is therefore the projected bubble area rather than the volumetric swelling.

The onset of bubble coalescence may be understood on the basis of a simple argument adapted from the work of Chandrasekhar [9] who calculated the distribution of nearest neighbours in a random three-dimensional distribution of particles. For a two-dimensional array, the argument runs as follows. Let $\omega(r)\,dr$ denote the probability that the nearest neighbour to a bubble occurs between r and $r + dr$. This probability must be equal to the probability that no bubbles exist interior to r multiplied by the probability that a bubble resides in the circular annulus between r and $r + dr$. Accordingly, the function $\omega(r)$ must satisfy the following relation:

$$\omega(r) = \left[1 - \int_0^r \omega(r)\,dr\right]2\pi rN, \tag{4}$$

where N is the number of bubbles per unit area of grain face. Solution of Eq. (4) yields

$$\omega(r) = 2\pi rN e^{-\pi r^2 N}. \tag{5}$$

The mean nearest neighbour distance is therefore

$$\bar{r} = 2\pi N\int_0^\infty r^2 e^{-\pi r^2 N}\,dr = (\pi N)^{-1/2}\Gamma(3/2) = 0.88623\cdot(\pi N)^{-1/2}. \tag{6}$$

Coalescence will occur when the radius of the bubble exceeds half the mean nearest neighbour distance, that is $r_{crit} > \bar{r}/2$. This will occur when the fractional coverage is equal to $\pi N r_{crit}^2$, which is equal to 19.6%.

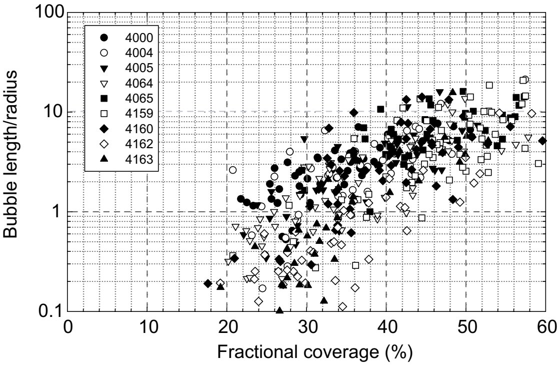

Fig. 5. Variation of the bubble aspect ratio (length/radius) with fractional coverage. Increases in bubble length begin to occur when the fractional coverage exceeds 17–18% in agreement with statistical models of coalescence on plane surfaces.

Fig. 5 shows the development of the bubble aspect ratio, that is, the ratio of the equivalent body length (L_p) to the projected radius (R_p) as a function of the fractional coverage. It can be seen that the bubble development is different for each particular experiment but that the earliest onset of bubble elongation occurs for fractional coverages around 17–18% and this is consistent with the 19.6% calculated above.

Once coalescence commences, its subsequent development may be calculated as follows. Each bubble will be surrounded by an area of, on average, four times its own area, A, in which no other bubble centres can reside. It is easy to demonstrate that this is correct for circular bubbles. The argument here is thought to be correct for identical bubbles of irregular shape. It is probably not true for a population of different size bubbles. Any bubble centre located in this exclusion zone would find its perimeter within the perimeter of the parent bubble and coalescence would occur. Any further growth of the projected area of the parent bubble by an amount dA, effectively increases the area of the exclusion zone by 4dA and opens the possibility that 4NdA bubble centres may be swept out. In that event the bubble perimeters will interact and coalescence occurs. Considering each bubble in turn, the total rate of loss of bubbles by coalescence following an increase in area is given by

$$\frac{dN}{dA} = -2N^2, \tag{7}$$

where the factor of 4 is reduced to 2 to avoid counting each interaction twice. Eq. (7) may be integrated to yield,

$$N = \frac{N_0}{1 + 2N_0(A - A_0)}, \tag{8}$$

where N_0 and A_0 are the initial density and projected area of the newly nucleated bubble population. Since the fractional coverage F_c is equal to NA it can be seen that the coalescence model predicts that the fractional coverage saturates at a value of 50%, very close to the observed value. Less than 10% of all grain boundaries examined have fractional coverages in excess of 50%.

The measured bubble densities are plotted as a function of the mean bubble areas for all boundaries in Fig. 6. It can be seen that most of the experimental data sit to the left of the model predictions. This is because coalescence occurs when the bubble area has increased to a value where it crosses the line defined by Eq. (8). Following coalescence, the bubble area shrinks as it attempts to minimise its surface area and moves leftwards. A number of data points are to the right of the line representing cases where the fractional coverage exceeds 50% but in no instance does the fractional coverage ever approach a value of $\pi/4$ (78.5%) which is often assumed to be the coverage at grain-face saturation [10].

At the point of coalescence, the projected shape of the new bubble will be that of two circles just touching. A narrow meniscus of high curvature will form at the point of contact. Material will flow from this region of high curvature to regions of lower curvature until there are no curvature gradients across the bubble surface. Given sufficient time, the final stable bubble shape will be that of a larger lenticular bubble of circular projection. However, in practice, the bubble shape will depend on the relative rates of bubble growth and morphological relaxation. Bubble growth depends on the fission gas arrival rate and the grain-boundary diffusion rates of vacancies. Bubble growth drives the coalescence process so it is obvious that the final shapes depend on whether morphological relaxation can occur before further growth and coalescence occurs.

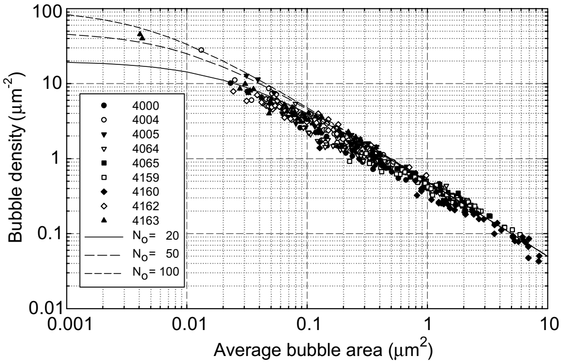

Fig. 6. Variation of the measured bubble density with mean bubble projected area. The lines are calculated from the coalescence model – Eq. (8) – with different initial values of bubble density. This figure reveals a universal trend for all data.

4.4. Morphological relaxation

4.4.1. The rate-limiting process

It is clear from Fig. 5 that without morphological relaxation, extremely long bubbles could form. Since the venting of fission gases to the grain edges depends critically on the average bubble length compared to the grain-face dimensions, it is important to attempt to understand the dynamics of the growth–coalescence–relaxation process on a mechanistic basis.

The driving 'force' for morphological relaxation will be the need to reduce the free energy of the cavity by a reduction in its surface energy. There are two structural components to the free energy; the first is the contribution from the surface area of the bubble and the second is that from the grain-boundary area occupied by the bubble. The two contributions have different surface energies associated with them but the equilibrium situation is that of a lenticular bubble of circular projection on the grain boundary.

In a previous analysis [11] it was assumed that surface diffusion provided the limitation to the morphological relaxation, that is, material diffused across the surfaces. Finite difference calculations were performed using the Nichols and Mullins equation [12]. For the example of an elongated bubble of length $L_p = 8$ and $R_p = 1$, full equilibration of the bubble occurred after a time given by

$$t \approx \frac{3kTR_p^4}{D_s \gamma_{fs} \Omega^{4/3}}. \tag{9}$$

For a specific example of bubbles of 200 nm radius at 2000 K, Eq. (9) indicates that full equilibration occurs in a time of about 2 min, while at 2200 K equilibration would occur in 10 s. These calculations are based on the use of the surface-diffusion coefficients derived by Maiya [13] and Reynolds [14] and clearly indicate that elongated bubbles should not be observed in UO_2 if morphological relaxation proceeds under surface-diffusion limited conditions.

An alternative mechanism for the shape-change could arise from an 'evaporation–condensation' mechanism in which atoms were evaporated from a region of high curvature and condensed in a region of lower curvature. This could be just as effective as surface diffusion although it may not operate at low temperatures or in the absence of a temperature gradient. Both mechanisms provide a means of bubble shape-change but they may not limit the rate at which it occurs, particularly in oxide fuels. The main reason for this is that the bubbles are associated with the grain boundaries and a change of shape from an elongated bubble to a circular bubble involves the recovery of some areas of grain boundary and the loss of other areas – see Fig. 7. This process requires the absorption or emission of lattice vacancies and may involve either diffusion of vacancies across the grain boundary – that is, grain-boundary diffusion – or diffusion through the bulk material – that is, lattice diffusion.

At the temperatures associated with the swelling process, it is likely that the shape-changes occur by a mechanism of surface diffusion. The big difficulty is that this process could terminate because the de-pinning of the grain boundary via vacancy absorption/emission takes place at a slower rate and the completion of the process depends on this slower rate process. As long as the absorption/emission of vacancies is slower that the internal process of shape-change, i.e. surface diffusion or evaporation–condensation, any shape-changes will occur almost instantaneously compared to the de-pinning of the bubble where it meets the grain boundary. The rate of the process is limited by whichever vacancy mechanism provides the source or sink of vacancies most rapidly. This is likely to be associated with the grain-boundary diffusion of vacancies.

4.4.2. Vacancy absorption/emission at grain-boundary cavities

The Speight and Beere equation [7] describes the flow of vacancies to a cavity under conditions in which the generation rate of vacancies balances all the other normal stresses on the boundary. It does not describe the rate of absorption at various points around the circumference of the bubble. It is clear, however, that the only factor that varies around the circumference is likely to be the bubble capillarity, i.e. its curvature, because the internal pressurisation and the applied stress will be independent of position. In order to study the variations around the cavity it is necessary to derive a new equation, which incorporates the azimuthal variation of the capillarity.

If we assume that a cavity of radius R_i sitting in a diffusion cell of radius R_0 with no generation of vacancies in the diffusion cell, the vacancy concentration in the cell is given by the solution to

$$\frac{D_g}{r}\frac{\partial}{\partial r}\left(r\frac{\partial c}{\partial r}\right) = 0. \tag{10}$$

This has to be solved such that the vacancy concentration at the boundary of the cavity is c_r while that at the boundary of the diffusion cell is equal to c_0. Under these conditions the radial variation of the vacancy concentration is given by

$$c = \left(\frac{c_0 - c_r}{S'}\right)\ln(r) + \text{const} \tag{11}$$

where

$$S' = -\frac{1}{2}\ln(F_c).$$

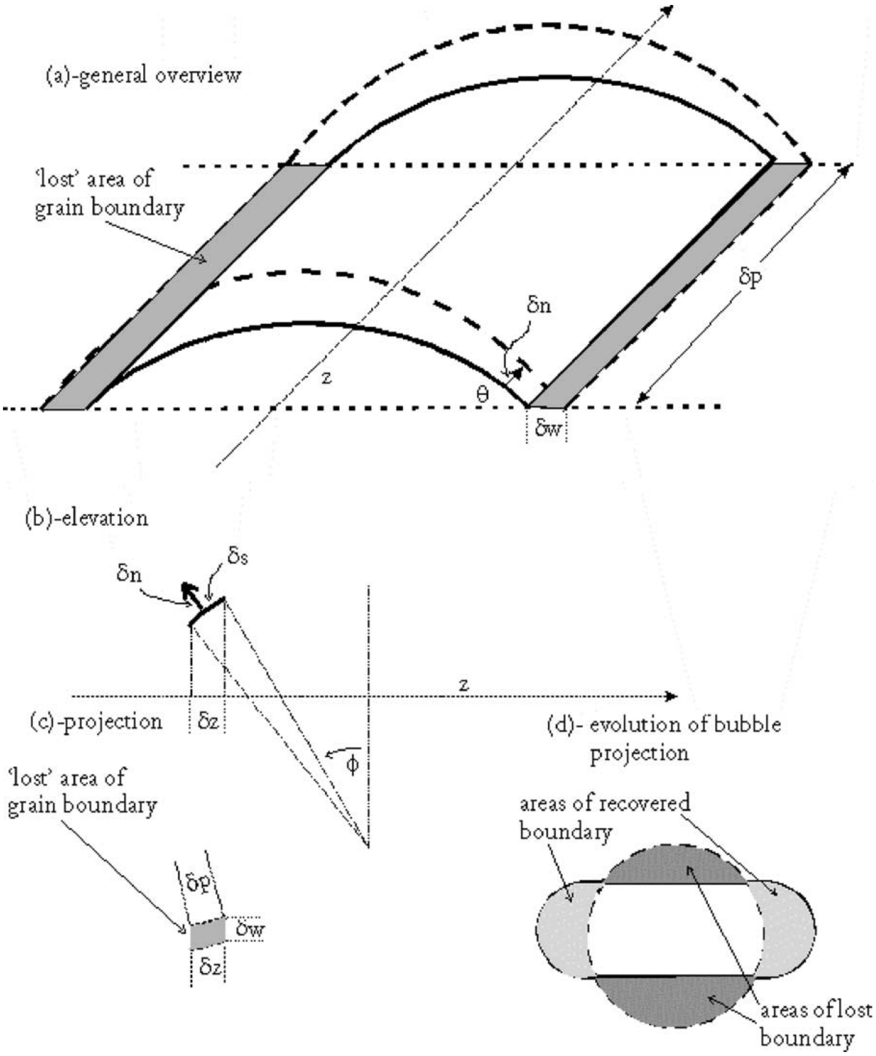

Fig. 7. Geometric details of the construction of a surface-of-revolution to approximate to grain-face porosity: (a) demonstrating how grain-boundary area is lost during local bubble growth, (b) the elevation of an element of surface and how this moves normally to the surface vector during bubble growth, (c) the projection of the surface element onto the grain boundary showing the relationship between the changes in width, length and perimeter, (d) showing the areas of lost and recovered grain boundary during bubble equilibration.

The flux into the cavity is given by

$$J = 2\pi D_g \delta_g R_i \left.\frac{\partial c}{\partial r}\right|_{r=R_i} = \frac{2\pi D_g \delta_g (c_0 - c_r)}{S'}. \tag{12}$$

The equilibrium concentration c_r associated with the bubble depends on its local value of curvature, κ, and may be written as

$$c_r = c_t e^{\frac{\kappa\gamma_{fs}\Omega}{kT}} \quad \text{which may be approximated to} \quad c_r \approx c_t\left(1 + \frac{\kappa\gamma_{fs}\Omega}{kT}\right). \tag{13}$$

If the perimeter of the bubble is P, then the flux into an element of the perimeter of length δP_i is equal to

$$J(\delta P_i) = \frac{2\pi D_g \delta_g}{S'}\left(c_0 - c_t\left(1 + \frac{\kappa_i\gamma_{fs}\Omega}{kT}\right)\right)\frac{\delta P_i}{P}, \tag{14}$$

where κ_i is the curvature of the surface at the perimeter element δP_i.

The net emission/absorption around the cavity is equal to zero because the generation rate within the diffusion cell is equal to zero. This can be calculated by summing all perimeter elements and equating to zero.

Under these conditions the boundary concentration, c_0, can be written as

$$c_0 = c_{\mathrm{t}}\left(1 + \frac{\overline{\kappa}\gamma_{\mathrm{fs}}\Omega}{kT}\right), \tag{15}$$

where $\overline{\kappa}$ is the average value of curvature around the perimeter. The local flux to each perimeter element can be calculated by substituting Eq. (15) into Eq. (14), to yield

$$J(\delta P_i) = \frac{2\pi D_{\mathrm{g}}\delta_{\mathrm{g}}\gamma_{\mathrm{fs}}\Omega}{kTS'}(\overline{\kappa} - \kappa_i)\frac{\delta P_i}{P}. \tag{16}$$

In Eq. (16), the additional c_{t} term, that is, the thermodynamic equilibrium vacancy concentration on the grain boundary, has been subsumed into the grain-boundary diffusion coefficient, D_{g}. Eq. (16) states the differential absorption/emission rates of vacancies, around the perimeter of a cavity as a function of the local value of curvature. It is a statement that the net absorption/emission is equal to zero and that the only source of vacancies on the boundary arises from the differential absorption/emission. It is for the reason that the net generation rate is zero that the S' term differs from the S term in Eq. (1). The boundary condition in Eq. (1) required the balancing of externally applied stresses by the generation/absorption of vacancies and this gave rise to the form of S.

4.4.3. Morphological relaxation through differential absorption/emission of vacancies

For surface-curvature driven shape changes to occur, sufficient vacancies must be either emitted or absorbed to pin or de-pin the grain boundary. The pore geometry is shown in Fig. 7 where the normal movement δn of an element of surface of length δs is considered. This element projects onto the boundary an area of 'lost' or 'recovered' boundary of width δw and longitudinal extent δz. (Note that δz differs from the perimeter δP.) The surface of revolution meets the boundary at the semi-dihedral angle, θ, so the normal rate of movement of the surface element can be related to the requirement that sufficient vacancies are absorbed/emitted to plate a monolayer in the parallelogram defined by $\delta P \cdot \delta z$. This is given by

$$\frac{\mathrm{d}n}{\mathrm{d}t} = \frac{B}{P\cos\phi}(\overline{\kappa} - \kappa)\frac{\mathrm{d}P}{\mathrm{d}z}, \tag{17}$$

where

$$B = \frac{1-\cos\theta}{\sin\theta}\cdot\frac{2\pi D_{\mathrm{g}}\delta_{\mathrm{g}}\gamma_{\mathrm{fs}}\Omega^{2/3}}{kTS'}.$$

This is the morphological relaxation equation when shape-change rates are limited by vacancy absorption/emission at the grain boundary. It relies on the fact that the surface-diffusion rates around the interior of the cavity occur very much faster and that as soon as the grain boundary region is de-pinned, shape-changes occur virtually instantaneously.

4.4.4. Application to morphological relaxation

Two situations are of relevance to shape-changes. These are (a) the kinetics of shape-changes immediately following bubble coalescence, and, (b) the shrinkage rate of well-developed elongated cavities. Both of these problems were addressed using the Nichols and Mullins equation [12] for surface diffusion controlled shape-changes in [11]. The difference between these calculations and the surface-diffusion limited cases is that the grain-boundary diffusion controlled cases are not volume conserving. This is because the net 'footprint' of the bubble decreases during equilibration and so more grain-boundary area is recovered than lost. This means that full equilibration is accompanied by a volume change.

As in the case of the Nichols and Mullins equation [12] it is more convenient to solve Eq. (17) in dimensionless variables. Making the following substitutions:

$$Y = \frac{y}{M}, \quad K = \kappa\cdot M, \quad N = \frac{n}{M}, \quad Z = \frac{z}{M},$$
$$Q = \frac{P}{M}, \quad \tau = \frac{Bt}{M^3},$$

where M is a scaling parameter with dimensions of length. The differential equation then becomes

$$\frac{\mathrm{d}N}{\mathrm{d}\tau} = \frac{1}{Q\cos\phi}\cdot\left(\overline{K} - K\right)\frac{\mathrm{d}Q}{\mathrm{d}Z} \tag{18}$$

and all physical parameters have been subsumed into the dimensionless time variable, τ.

Eq. (18) has been solved using standard finite difference methods [15,16]. The bubble is treated as a surface of revolution and is generated as a series of Z–Y co-ordinates and values of K are evaluated using 3-point discretisations. The profile is regenerated at intervals to maintain spacing between the Z–Y co-ordinate points.

4.4.5. Post-coalescence shape-changes

The simplest example of coalescence can be found when two bubbles of circular projection meet. The initial projected shape is that of a 'figure-eight' with a sharp cusp in the middle. This abrupt change in curvature acts as a strong sink for vacancies enabling material to flow away to regions of lower curvature. The kinetic behaviour of bubble coalescence is shown in Fig. 8 for interactions between bubbles of various initial aspect ratios. The newly coalesced bubble can be seen to have equilibrated when the overall length and the width are equal, that is, the bubble has a circular projection.

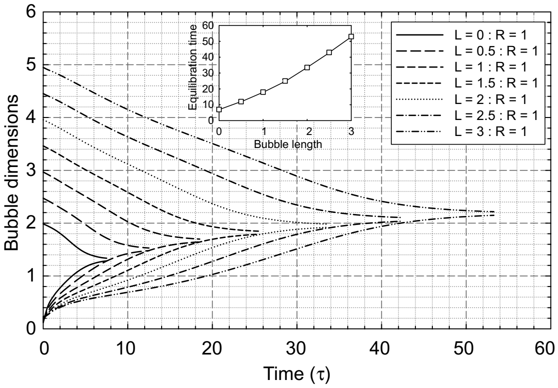

Fig. 8. The kinetics of the coalescence of elongated bubbles under grain-boundary limited conditions. The parameters shown are the overall bubble length and the mid-point width. These necessarily converge on the same value, that is, the resulting bubble has circular projection. Note that the coalescence event is stable for all cases considered. All parameters in this plot are dimensionless.

Since the 'τ' scale subsumes all the physical parameters for the process, the actual timescale depends on the true bubble dimensions and the diffusion coefficient. The equilibration time increases as the third power of the bubble radius, in contrast to the situation with surface diffusion control, which increases as the fourth power and because of the dependence on diffusion coefficient, the equilibration time would decrease with temperature. The final shapes of the bubbles clearly depend on the relative rates of growth, coalescence and shrinkage. For example, if growth occurs rapidly, then further coalescence may occur before the bubbles have returned to their equilibrium shapes. In this way, there may be a steady increase in the bubble length and future coalescence events may take place between non-equilibrium bubbles. In this instance 'equilibrium' refers to the state where the bubble projection is circular, rather than the state of equilibrium when the internal pressure and the capillarity are in balance. This latter situation seldom occurs in irradiated UO_2.

The detailed morphological changes for the coalescence of two initially elongated bubbles is illustrated in Fig. 9. It should also be observed how examples of the calculated shapes in Fig. 9 are observed under irradiation conditions in Figs. 3 and 4.

4.4.6. Bubble shrinkage

The situation shown in Fig. 9 for $\tau = 28$ shows an idealised elongated bubble. This bubble can be created by cutting an equilibrium lenticular bubble in two and inserting a prismatic section to link the two parts. The bubble may be described by its projected radius, R_p, and its body length, L_p and is used to characterise intergranular pores. It is the shrinkage of this type of bubble that concerns this section.

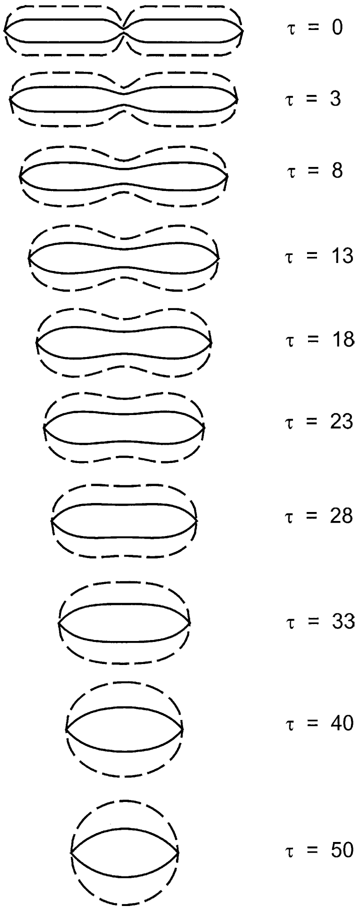

Fig. 9. Plan and elevation views of the morphological changes following the coalescence of two bubbles with $L_p/R_p = 3$ at various stages under conditions of grain-boundary limitation. Note that full relaxation takes much longer than for two circular bubbles.

The plan and elevation shape-changes for a bubble in which $L_p = 8$ and $R_p = 1$ are shown in detail in Fig. 10 and the kinetics are illustrated in Fig. 11. For use in fuel modelling codes it is desirable to be able to treat the shrinkage process using a simple algorithm rather than solving Eq. (18) for each individual case. Fig. 11 shows that the initial shrinkage rates are linear with identical slope for all bubble lengths. However, the formal similarity of Eq. (16), which determines the shrinkage rate and Eq. (1), which determines the swelling rate, suggests that the shrinkage rate will also depend on the swelling rate. Combining the two equations reveals that this effect may be investigated by replacing the $\overline{\kappa}$ term by $\alpha\overline{\kappa}$, where α is a multiplier which enhances the swelling rate.

In Fig. 12 it can be that the initial shrinkage rates are proportional to the swelling rate, that is, as the swelling

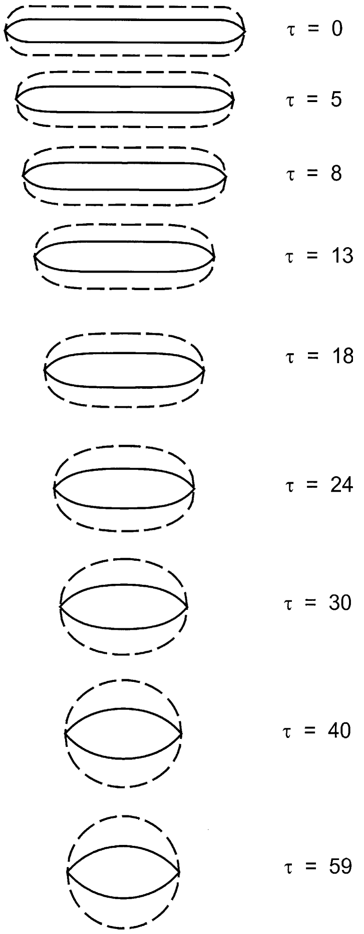

Fig. 10. Plan and elevation views of the morphological changes during the shrinkage of a long bubble under conditions where shape-change is limited by the loss and recovery of grain-boundary area.

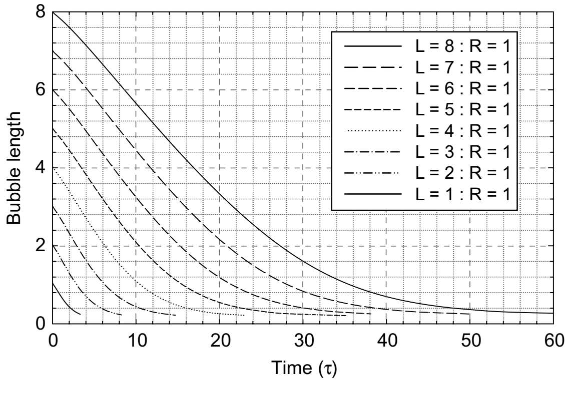

Fig. 11. Kinetics of bubble shrinkage under conditions where shape changes are limited by the loss and recovery of grain-boundary area.

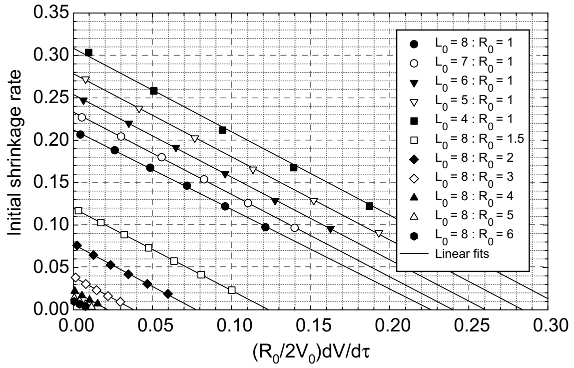

Fig. 12. The initial shrinkage rate of elongated bubbles under grain boundary limited shape-change as a function of bubble growth rate for a range of bubble geometries.

rate increases, the shrinkage rate decreases. At some stage the swelling rate will reach a value such that the bubble will elongate rather than shrink. The proportionality between the two rates may be described by

$$\frac{\mathrm{d}L}{\mathrm{d}\tau} = -\alpha_1 + \alpha_2 \frac{\mathrm{d}V}{\mathrm{d}\tau}, \tag{19}$$

where

$$\alpha_1 \approx \frac{7.26 L_{\mathrm{p}0} R_{\mathrm{p}0}}{Q_0 V_0} \quad \text{and} \quad \alpha_2 = \frac{R_{\mathrm{p}0}}{2V_0}.$$

In Eq. (19) the ‘0’ suffix refers to initial values of the dimensionless variables. τ is defined in normalising process leading to the derivation of Eq. (18) and L_{p}, R_{p}, Q and V are the length, projected radius, bubble perimeter and volume, respectively. A consequence of Eq. (19) is that because the swelling rate can be suppressed by large hydrostatic stresses – see Eq. (1) – this would also have an effect on the shrinkage rate of bubbles.

4.5. Grain-face venting

The fraction of the grain-face porosity that is vented to the grain edges was measured for all complete boundaries. The vented fraction varies from values of around zero and in some cases attains a value of 100% indicating that all of the gas that has arrived at the boundaries has been vented to the grain edges and probably escaped to the fuel exterior. The vented fraction is low for small fractional coverages and only appears to increase significantly when the aspect ratio of the bubbles increases. This would indicate that the vented fraction might, in some way, depend on the statistical probability of an elongated bubble intersecting the bounding perimeter of the grain face.

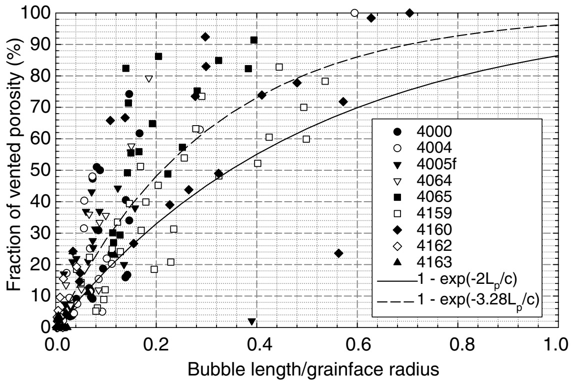

Fig. 13. Measured values of the fraction of vented porosity as a function of the ratio of bubble length to grain-face radius. Note that the simple model is improved by a modification of the coefficient.

For the case of a circular grain face of radius, *c*, we can consider an array of bubbles of length L_p and radius R_p of which m_v are vented and m_{nv} are non-vented. The conversion rate from non-vented to vented depends on the number within a distance R_p of the grain edge, that is, within a distance R_p of the perimeter of a circle of radius '*c*'. A small change in the bubble length L_p will cause venting at a rate

$$\frac{dm_v}{dt} = \frac{2\pi(c - R_p)}{\pi c^2} m_{nv} \approx \frac{2m_{nv}}{c}. \qquad (20)$$

The vented fraction $F_v = m_v/(m_v + m_{nv})$, so, substituting in Eq. (20) and integrating, yields

$$F_v = 1 - e^{-\frac{2L_p}{c}}. \qquad (21)$$

The vented fraction data are shown in Fig. 13 and are reasonably well described by the functional form of Eq. (21). A better description is, however, provided by increasing the coefficient in the exponential from 2 to 3.28. This is, perhaps, not too surprising given the simplicity of the argument leading to Eq. (21), which ignores the possibility of bubbles nearer the centre of the grain-face impacting on bubbles which themselves are already in contact with the grain-edge.

5. Synthesis of inter-granular swelling model

The driving force for grain-boundary swelling is the arrival of fission gas at the grain boundaries. This is calculated using the standard Booth [17] method along with the time-stepping algorithm described in [18]. The diffusion coefficient conforms to the Turnbull three-term formulation [19,20] and compensation for the effects of intra-granular porosity is modelled using the revisions proposed in [21]. The effects of irradiation induced re-solution from the grain-boundary porosity are included in the model but are, in fact, of little consequence at the temperatures of the experiments under consideration.

5.1. Included elements

A nucleation density of 20 μm^{-2} is assumed. Experiments with values between 10 and 50 suggest that the actual value is not too critical since, it is clear from Fig. 6 that once swelling commences the value falls very quickly.

The following calculational sequence is adopted:

(i) The bubble growth rate is calculated using the Speight and Beere [7] equation driven by fission gas release to the grain boundaries.
(ii) Morphological changes are calculated using the swelling dependent shrinkage rate to provide values of bubble length and radius consistent with the new bubble volume.
(iii) The loss of bubble density through coalescence is calculated using the new projected bubble area after the combined effects of growth and morphological relaxation. The newly coalesced bubble is assumed to retain the same projected radius.
(iv) The fraction of vented porosity is calculated from the ratio of the bubble length to the equivalent grain-face radius.
(v) If the vented fraction increases during the time-step, the excess fission gas is released.

5.2. Power-history simulation

The input parameters for the model are the time-step duration, the rating, the fuel temperature and the applied hydrostatic stress restraining cavity growth. These parameters were obtained for each fuel location by interpolating the output from an ENIGMA [1,3] calculation at the appropriate radial position of the fuel sample. The ratings were obtained from Halden power calibrations and are accurate to within ±5% while the temperature calculations are expected to be within ±50 °C.

5.3. Optimisation of diffusion coefficients

Grain-face swelling and bubble morphology depend critically on the value of the grain-boundary diffusivity. The shape-changes occurring in UO_2 are incompatible with accepted values of surface diffusivity and an alternative shape-change equation has been derived based on absorption and emission of vacancies at the grain-boundary/bubble interface. In order to check whether this approach is valid, the fitting process has been performed assuming separate values of grain-boundary diffusivity for the two processes, that is, a value for growth and an independent value for morphological relaxation.

The results for the two values of grain-boundary diffusivity are shown in Fig. 14. It is clear that the values required for bubble growth and morphological relaxation are nearly identical so it can be assumed that diffusion of vacancies from the grain boundaries controls both processes. This is consistent with the observation that surface diffusion occurs extremely rapidly and that morphological relaxation is not controlled by surface diffusion on the bubble interior but by the necessary readjustments required to create and destroy grain boundary.

The results reported by Reynolds and Burton [22] obtained from analysis of creep and sintering data are also displayed in Fig. 14. There is a difference in activation energy between the present results and those obtained by Reynolds and Burton but this may be illusory because their activation energy was obtained from the composite dataset. If the datasets are considered separately – see the broken lines in Fig. 14 – the activation energies of all datasets can be seen to be virtually identical. The shift in magnitude between the various experiments probably reflects the analytical methods employed. For example, the present data were analysed using the Speight and Beere [7] equation while the Reynolds and Burton [22] results employed the Hull and Rimmer equation [8]. It is not possible to compare the analyses retrospectively because Reynolds and Burton do not give details of the porosity distributions in their specimens.

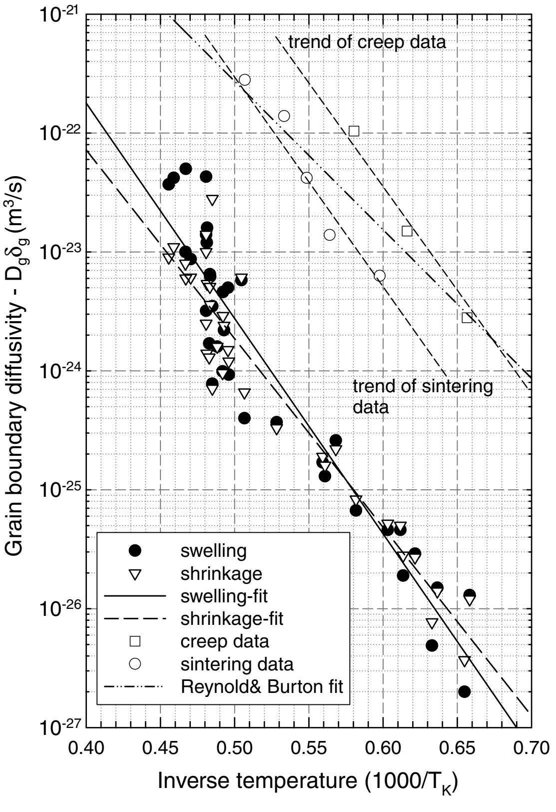

Fig. 14. Optimised values of the grain-boundary diffusion coefficient appropriate to the results from the in-pile tests. The data sit below the previous estimates of Reynolds and Burton [22] but this is probably a result of their use of the Hull and Rimmer [8] formulation. Note that the values of diffusivity required for bubble growth and morphological relaxation are virtually identical indicating the validity of the shrinkage mechanism.

6. Model performance

6.1. The swelling database

The stand-alone gas release and swelling model incorporates the features described in Sections 4 and 5 and calculates the evolution of the projected radius and length of the average bubble, the density of bubbles on the grain faces and the overall grain-face swelling. The results of these calculations are summarised in Figs. 15–18. The following comments can be made.

The bubble radii are reasonably well modelled over the entire range from 100 to 600 nm with slight overprediction at the lowest levels – see Fig. 15. The error bars on the radius measurements are quite small indicating a degree of uniformity between the various specimens. In contrast, the experimental error bars on the bubble lengths are very large – Fig. 16. This reflects the fact that the grain faces are usually decorated with a range of bubbles in various states of growth and coalescence – see Fig. 4, for example. The theoretical model treats the bubble population as a homogeneous population of identical bubbles so the predictions tend to look less impressive than those for the bubble radii.

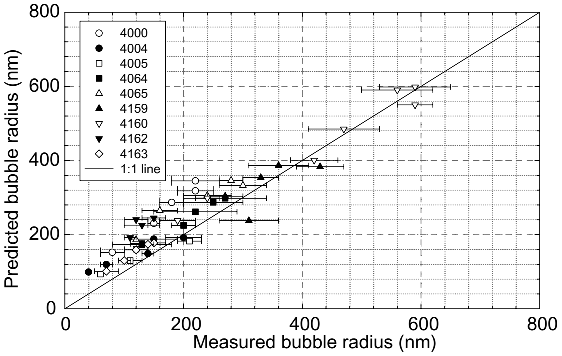

Fig. 15. Predicted projected bubble radii compared with the measured values from the in-pile tests.

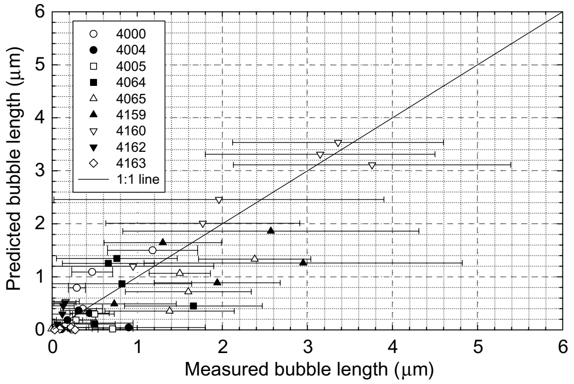

Fig. 16. Predicted projected bubble lengths compared with the measured values from the in-pile tests.

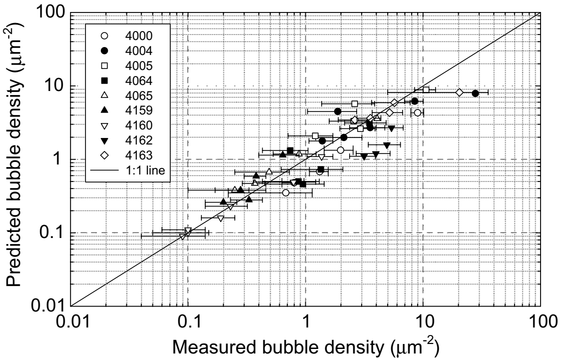

Fig. 17. Predicted bubble densities compared with the measured values from the in-pile tests.

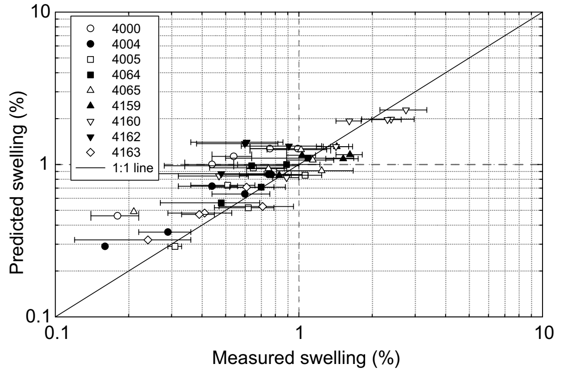

Fig. 18. Predicted volumetric swellings compared with the measured values from the in-pile tests.

Fig. 17 shows the bubble densities and agreement is good over a range of two orders of magnitude. The error bars reflect the standard deviation of the measured bubble densities and are generally about 25–50% of the measured value. The only real deficiencies in the predictions occur at high bubble densities and this is also the region where the bubble radius is slightly overpredicted so the two problems are related. Finally, Fig. 18 shows the total grain-face swelling and this is a result of the combination of the predictions of the radii, lengths and densities. Overall the agreement is satisfactory although there are areas where improvements could be sought, particularly in the 0.5–1.0% swelling range where the values are overpredicted.

One area of difficulty in these calculations is associated with the coalescence model. Eqs. (7) and (8) predict a saturation of the grain boundaries at 50% coverage but about 10% of all boundaries exhibit coverages between 50% and 60%. The model calculations usually predict near-saturation values of coverage even when the measured values are around 30–40% suggesting that modifications to Eq. (7) could be usefully made. This is probably the principal source of the overprediction of the swelling in the 0.5–1.0% region.

6.2. The effects of hydrostatic stress and bubble overpressure

Swelling calculations for case 4000, which was subjected to a fast ramp followed by a 30-min hold at peak ratings, indicate that the grain boundary cavities contain approximately 18 vacancies per atom, that is, only about 5% of the swelling is provided by fission gas atoms. The predicted projected bubble radius for this calculation is approximately 350 nm and for a bubble of this size to be in mechanical equilibrium with the capillarity, there should be around 600 vacancies per atom rather than the 18 calculated. The calculated value is very similar to that estimated from post-irradiation annealing experiments by assuming a quasi-crystalline model for grain-boundary bubbles [23]. In addition, the internal pressure of the bubbles may be calculated using Eq. (2) and this is approximately 39 MPa at 1800 °C, a value which is very close to the 35 MPa calculated by Brohan [24] using different methods.

The internal pressurisation of the bubbles calculated above indicates that the bubbles are a long way from equilibrium. The pressures are also in excess of the hydrostatic stresses calculated using the ENIGMA program [1,3], for example, for the case studied above the compressive stress at the peak of the ramp was approximately 15 MPa. The compressive stresses in LWR fuel, which employs solid rather than hollow pellets, are likely to exceed those experienced in AGR fuel, possibly reaching values of around 100 MPa in transients. These greater stresses are likely to constrain the swelling and lead to higher bubble internal pressures and to greater storage on the grain boundaries but are of such magnitudes as to be unlikely to invalidate the bases of the swelling model.

These calculations have far-reaching consequences in that the application of physically based models to cavity growth and nucleation predicts that the grain-boundary bubbles are highly over-pressurised, even at high temperatures: this has always been suspected to be the case. The example discussed, demonstrates that at low temperatures the bubble over-pressure can be very high and large amounts of gas may be stored on the boundaries in what appears to be an array of very small cavities. Subsequent excursions to even moderate temperatures will lead to increasing vacancy generation and mobility which in turn will increase the swelling and subsequent release of gas to the grain edges. This may occur as a result of the gas already residing on the boundaries without need of any additional diffusion from within the grains. Thus attempts to explain what is referred to as 'burst-release' on the basis of intra-granular fission gas diffusion are wide of the mark because the gas is already technically released from within the grains. Under these conditions the 'burst-release' process is entirely dominated by the vacancy diffusivity on the grain boundaries although there will, of course, eventually be additional contributions from intra-granular diffusion.

7. Conclusions

A number of separate studies have provided a large database of information on grain-boundary swelling. The key parameters of bubble dimensions and morphology in conjunction with bubble densities and total swelling on 427 separate grain boundaries has enabled a thorough systematic study of the swelling phenomenon in UO_2. In addition, power histories of the test rods were sufficiently well defined to enable ENIGMA calculations to be performed, yielding temperature and rating histories for the locations from which SEM specimens were obtained.

A model for grain-boundary swelling has been developed based on five separate features. These are:

(i) Initial one-off nucleation at a fixed density. There is evidence that nucleation continues during the irradiation but the small bubbles provide insignificant swelling compared to the maturing initial population so the approximations made by the one-off assumption are small.
(ii) Bubble growth through fission gas atom collection causing over-pressure driven bubble growth. It has been demonstrated that vacancy generation and migration on the grain boundaries is the rate-determining process.
(iii) Coalescence of bubbles according to a simple random interference model. This process can give rise to elongated bubbles.
(iv) Following coalescence, the elongated bubbles undergo a growth-dependent morphological relaxation process through capillarity-induced surface diffusion. However, the process is limited by the rate at which the grain boundary can accommodate the new shape of the bubble through differential absorption and emission of vacancies.
(v) Venting of elongated pores to the grain edges with a phenomenological treatment of bubble-length/grain-edge intersection probability.

The model has been coded into a stand-alone gas release model and used to model the separate experiments from which the models were developed. The predicted swelling rates and bubble morphologies depend on the value of the grain-boundary diffusion coefficient as well as the fission gas release calculation. Reasonable agreement between predictions and measurement is obtained for the case of in-pile irradiations of UO_2 fuel.

Acknowledgements

The author would like to thank BNFL for support during the development of the work reported in this paper and to Paul Cook, Stan Fisher, Gary Gates and Ian Palmer for many constructive discussions during the past five years. Special thanks are also due to John Stump and Ken Stook of Berkeley Centre without whose contributions the SEM work would have been routine rather than inspired.

Appendix A. Grain-face swelling

The following relations are appropriate to lenticular pores with a semi-dihedral angle, θ.

The bubble projection on the grain boundary is defined by three numbers: R_p is the projected radius, L_p is the projected length, N_L is the number of lobes ($=2$ for circles and bilobes).

The volume of a lenticular bubble of circular projection is

$$V = \frac{4\pi R_p^3}{3} \cdot \frac{f_f(\theta)}{\sin^3\theta}, \tag{A.1}$$

where

$$f_f(\theta) = 1 - \frac{3}{2}\cos\theta + \frac{1}{2}\cos^3\theta.$$

The volume of the prismatic body of length L_p is

$$V_{body} = L_p R_p^2 f_p(\theta), \tag{A.2}$$

where

$$f_{\mathrm{p}}(\theta) = \frac{2\theta - \sin 2\theta}{\sin^2 \theta}.$$

The volume of a pore with N_{L} lobes is therefore given by

$$V_{\mathrm{P}}^{N} = \frac{N_{\mathrm{L}}}{2} a_1 R_{\mathrm{p}}^3 + a_2 R_{\mathrm{p}}^2 L_{\mathrm{p}}, \tag{A.3}$$

where

$$a_1 = \frac{4\pi f_{\mathrm{f}}(\theta)}{3\sin^3\theta} \quad \text{and} \quad a_2 = f_{\mathrm{p}}(\theta).$$

For bubbles of $\theta = 50°$, $a_1 = 1.571$ and $a_2 = 1.296$.

References

[1] R.J. White, R.C. Corcoran, J.P. Barnes, A Summary of Swelling Data Obtained from the AGR/Halden Ramp Test Programme, Report R&T/NG/EXT/REP/0206/02, 2002.

[2] P. Menut, E. Sartori, J.A. Turnbull, in: Proceedings of the ANS International Topical Meeting on Light Water Reactor Fuel Performance, Park City, Utah, USA, 2000, ISBN-0-89448-656-X.

[3] W.J. Kilgour, J.A. Turnbull, R.J. White, A.J. Bull, P.A. Jackson, I.D. Palmer, Capabilities and validation of the enigma fuel performance code, ANS/ENS Topical Meeting on LWR Fuel Performance, Avignon, France, 1991.

[4] C. Baker, J. Nucl. Mater. 66 (1977) 283.

[5] G.L. Reynolds, W. Beere, P.T. Sawbridge, J. Nucl. Mater. 41 (1971) 112.

[6] P. Van Uffelen, J. Nucl. Mater. 280 (2001) 133.

[7] M.V. Speight, W. Beere, Metal Sci. 9 (1975) 190.

[8] D. Hull, D.E. Rimmer, Philos. Mag. 4 (1959) 673.

[9] S. Chandrasekhar, Rev. Mod. Phys. 15 (1943) 1.

[10] T. Kogai, J. Nucl. Mater. 244 (1997) 131.

[11] R.J. White, in: Fission Gas Behaviour in Water Reactor Fuels, Cadarache, France, OECD, 2000, p. 189.

[12] F.A. Nichols, W.W. Mullins, J. Appl. Phys. 36 (1965) 1826.

[13] P.S. Maiya, J. Nucl. Mater. 40 (1971) 57.

[14] G.L. Reynolds, J. Nucl. Mater. 24 (1967) 69.

[15] W. Cheney, D. Kincaid, Numerical Mathematics and Computing, Brooks/Cole Publishing Company, Monterey, CA, 1985, ISBN-0-534-04356-9.

[16] R.L. Burden, J.D. Faires, Numerical Analysis, Prindle, Weber & Schmidt, Boston, 1985, ISBN 0-87150-857-5.

[17] A.H. Booth, A method of calculating fission gas diffusion from UO_2 fuel and its application to the X-2-f loop test, Report AECL 496, 1957.

[18] R.J. White, M.O. Tucker, J. Nucl. Mater. 118 (1983) 1.

[19] J.A. Turnbull, R.J. White, C. Wise, in: Proceedings of the IAEA Technical Committee Meeting on Water Reactor Fuel Element Computer Modelling in Steady-State, Transient and Accident Conditions, Preston, UK, 1988, IAEA-TC-659/3.5, p. 174.

[20] R.J. White, J. Nucl. Mater. 295 (2001) 133.

[21] R.J. White, in: Proceedings of the IAEA Technical Committee on Nuclear Fuel Behaviour Modelling at High Burn-Up and Its Experimental Support. Lake Windermere, UK, 2000, IAEA-TECDOC-1233.

[22] G.L. Reynolds, B. Burton, J. Nucl. Mater. 82 (1979)22.

[23] R.J. White, in: BNES Meeting on Fuel Management and Handling, Edinburgh, 1995, p. 218.

[24] P. Brohan, in: Proceedings of the ANS International Topical Meeting on Light Water Reactor Fuel Performance, Park City, Utah, USA, 2000, ISBN-0-89448-656-X.